The Journal of Chemical Physics

High-sensitivity fluorescence-detected multidimensional electronic spectroscopy through continuous pump–probe delay scan

Cite as: J. Chem. Phys. **158**, 024201 (2023); https://doi.org/10.1063/5.0130887
Submitted: 15 October 2022 • Accepted: 19 December 2022 • Accepted Manuscript Online: 19 December 2022 • Published Online: 09 January 2023

Amitav Sahu, Vivek N. Bhat, Sanjoy Patra, et al.

The Journal of Chemical Physics ARTICLE scitation.org/journal/jcp

High-sensitivity fluorescence-detected multidimensional electronic spectroscopy through continuous pump–probe delay scan

Cite as: J. Chem. Phys. 158, 024201 (2023); doi: 10.1063/5.0130887
Submitted: 15 October 2022 • Accepted: 19 December 2022 •
Published Online: 9 January 2023

Amitav Sahu, Vivek N. Bhat, Sanjoy Patra, and Vivek Tiwari[a)]

AFFILIATIONS

Solid State and Structural Chemistry Unit, Indian Institute of Science, Bangalore, Karnataka, 560012, India

Note: This paper is part of the 2022 JCP Emerging Investigators Special Collection.
[a)]**Author to whom correspondence should be addressed:** vivektiwari@iisc.ac.in

ABSTRACT

Fluorescence-detected multidimensional electronic spectroscopy (fMES) promises high sensitivity compared to conventional approaches and is an emerging spectroscopic approach toward combining the advantages of MES with the spatial resolution of a microscope. Here, we present a visible white light continuum-based fMES spectrometer and systematically explore the sensitivity enhancement expected from fluorescence detection. As a demonstration of sensitivity, we report room temperature two-dimensional coherence maps of vibrational quantum coherences in a laser dye at optical densities of ~2–3 orders of magnitude lower than conventional approaches. This high sensitivity is enabled by a combination of biased sampling along the optical coherence time axes and a rapid scan of the pump–probe waiting time T at each sample. A combination of this approach with acousto-optic phase modulation and phase-sensitive lock-in detection enables measurements of room temperature vibrational wavepackets even at the lowest ODs. Alternative faster data collection schemes, which are enabled by the flexibility of choosing a non-uniform undersampled grid in the continuous T scanning approach, are also demonstrated.

I. INTRODUCTION

Quantum mechanical couplings between overlapping vibrational-electronic manifolds dictate ultrafast energy and charge transfer. However, spectral congestion in the condensed phase can limit mechanistic insights into the origins of such couplings. Multidimensional electronic spectroscopy (MES) borrows concepts[1] from Fourier transform multidimensional nuclear magnetic resonance (NMR) experiments[2] to spectrally decongest femtosecond relaxation dynamics into an evolving two-dimensional (2D) contour map along the excitation and detection frequency axes. The resulting 2D spectrum can provide frequency resolution limited only by the system. Evolving contour map snapshots along the pump–probe waiting time T, with time resolution limited by the excitation pulses, are reporters of electronic relaxation, as well as fluctuating nuclear environments and molecular structures, which are frozen during a femtosecond excitation. MES has advanced the understanding of novel ultrafast processes by disentangling congested dynamics, such as those of polariton, plasmon, and molecular aggregate states in "plexitons"[3] to coherence, energy, or charge transfer in photosynthetic proteins and whole cells.[4]

Interferometric detection of a phase-matched signal has sensitivity limitations for scatter prone samples, such as whole cells.[5,6] Improvements in experimental techniques,[7] such as double chopping and spatially encoded time delays, have enabled scatter suppression to a certain extent. Action-based MES[8] is an alternative approach to MES, which promises high-sensitivity. For example, recent demonstrations[9,10] of action-based MES through the high-sensitivity detection of photoionization signals have opened a new paradigm in gas phase spectroscopy and motivate similar explorations in fluorescence-detected MES (fMES). fMES relies on the detection of fluorescence arising from non-linear wavepacket interferometry[11] to provide facile scatter suppression through optical filtering.

Demonstrations of fully collinear fMES through 125-step shot-to-shot phase cycling[12] have also led to the isolation of higher order non-linear signals. Acousto-optic phase modulation (AOPM) based dynamic phase cycling[13] or spatial light modulator (SLM) based

27-step phase cycling approaches to fMES are well suited for higher repetition rate broadband light sources and are more desirable for microscopy applications. Both approaches have demonstrated 2D coherence map (CM) measurements, which are typically challenging to measure at room temperature, and also paved way for spatially resolved fMES in a confocal geometry.[14,15] Non-collinear fMES has also been demonstrated[16] by imaging the dynamic population grating in the sample. The sensitivity of background-free fluorescence detection to measurements of weak nonlinear signals, such as vibrational coherences, at room temperature is expected to be high but not yet explored in either case. Parallels in 2DIR have already demonstrated[17] feasible measurements of vibrational couplings in a 2DIR spectrum at concentrations ~2× lower than typical upon fluorescence-encoding of vibrational excitations.

This article explores the sensitivity limits of the AOPM-based dynamic phase cycling approach to fMES. One way to improve sensitivity is through reductions in data collection time, such as the recent demonstration[18] of rephasing and non-rephasing 2D spectra at a single waiting time T through a rapid stage scan along the optical coherence axes. This demonstration is especially relevant in the context of spatially resolved measurements where other fMES approaches reported[8] so far have relied on two orders of magnitude higher repetition rates. Notably, a combination of white-light continuum (WLC) based experiments and lower repetition rates makes such an approach highly desirable but equally more challenging. Here, we demonstrate ~2–3 orders of magnitude higher sensitivity in fMES than conventional MES by considering an alternative rapid scan approach.

Rapid scan pump–probe experiments and theoretical modeling from Moon[19] have suggested that the rapid-scan approach leads to a higher signal-to-noise (SNR) ratio for high signal levels. Counterintuitively, in the case of weak signals with dominant probe-induced noise, higher SNR can be achieved with a fast lock-in time constant compared to rapid scanning (see Figs. 3 and 4 of Ref. 19). This is made possible by lock-in demodulation, minimizing the probe spectral noise density transferred to the signal. Furthermore, typically all fMES approaches so far have relied on scanning the delay axis grid uniformly even though noise fluctuations in data points close to zero delay affect the signal the most. Motivated by these considerations, we report a visible WLC-based fMES approach that relies on biased stepwise sampling along the optical coherence axes and continuous scanning of pump–probe delay (T) instead. The advantages of phase-sensitive lock-in detection in the AOPM approach are maintained because the T delay is rapidly scanned using a fast lock-in time constant. A continuous T scanning approach, that is, fine T sampling implemented here, is especially relevant for detecting weak coherences in WLC based setups, where light source stability across the entire bandwidth is typically lower[20,21] than that achievable through optical parametric amplification. Measurements with fine sampling along T are more robust to laser power drifts with $1/\sqrt{N}$ improvements, where N is the number of fine sampled T points. Furthermore, rapid scanning allows for more number of T averages necessary to break spectral and temporal correlations across the WLC bandwidth.[22] Additionally, stepwise sampling along optical coherence axes can be *biased* toward sampling uniform signal contours rather than grids. A crucial advantage of continuous T scanning per grid point is the ability to freely optimize the time window over which the sample is continuously exposed to light. Together, these innovations allow for unprecedented sensitivity improvements with the detection of room temperature CMs in a laser dye at ODs ~2–3 orders of magnitude lower than conventional MES approaches, along with signal isolation based on the T quantum beat phase. Our approach of the rapid scan along T and biased stepwise sampling along optical coherence axes harnesses the full potential of the AOPM approach through physical undersampling of optical coherences, is amenable to non-uniform sampling and signal reconstruction through compressive sensing algorithms,[23] and is relevant for measurements at lower repetition rates or with low count rate sources, such as entangled photon pairs.[24] Substantial reduction in the sample exposure window also makes the continuous T scanning approach highly desirable for spatially resolved measurements. The rapid T scanning approach presented here is well-suited for systems with fast optical dephasing and susceptibility to photodamage, with more general applications in AOPM-based coherence-detected[25–27] or photocurrent-detected[28,29] microscopy experiments.

II. EXPERIMENT AND METHODS

This section briefly discusses the theoretical background for the AOPM approach to fMES before describing our experimental approach. This is followed by a description of the data collection and analysis procedure.

A. fMES signal and acousto-optic phase modulation (AOPM)

Cina and Marcus detailed the formalism[11,13] for fMES in terms of non-linear wavepacket interferometry (WPI) experiments, originally pioneered by Scherer *et al.*[30] This formalism will be described briefly in the context of the AOPM approach implemented here.

Consider a two-level system with state kets $|g\rangle$, $|e\rangle$ representing the two electronic states. The initial state at $t = 0$ is $|g\rangle$. A first-order light–matter interaction at time t_1 results in the time-dependent state, $|\psi^{(1)}(t)\rangle = \frac{-i}{\hbar}\int_0^t e^{i\omega_e(t-t_1)}(-\hat{\mu}_{eg}\cdot\vec{E}(t_1))e^{-i\omega_g t_1}dt_1$, where $\hat{\mu}_{ge}$ is the transition dipole vector from ground state $|g\rangle$ to excited state $|e\rangle$ and ω_g, ω_e are the energy of the ground and excited state, respectively. Converting the above equation into a Fourier transform,[31] the probability amplitude transferred to the excited state after a first-order light–matter interaction is $\frac{i}{\hbar}\hat{\mu}_{eg}\cdot\vec{E}(\omega_{eg})$. In a WPI experiment, the probability amplitude arising from different light–matter interactions interferes to result in modulations of excited state population, recorded as modulating fluorescence signals. For example, wavepacket interferences between first-order wavepackets, such as $\left\langle\psi_1^{(1)}\middle|\psi_2^{(1)}\right\rangle$, lead to fluorescence signals that are linear with excitation intensity and depend on the relative delay between the two first-order interactions (at times t_1 and t_2 for $\vec{E}_1$ and $\vec{E}_2$, respectively). Note that the parentheses superscript denotes the order of interaction and the subscript denotes electric field labels. Only interference between wavepackets arising from *different* electric fields depends on the experimentally controllable time delay between their envelopes. In the same fashion, the non-linear wavepacket overlaps in fMES arise from interferences[13] such as $\left\langle\psi_{124}^{(3)}\middle|\psi_3^{(1)}\right\rangle$ and $\left\langle\psi_{134}^{(3)}\middle|\psi_2^{(1)}\right\rangle$ for ground state bleach (GSB) and excited state emission (ESE) signals, respectively.

The total electric field at a time t_1 can be written in the frequency domain as $\vec{E}_i(\omega) = e_i(\omega)e^{i\phi_i(\omega)}e^{i\omega t_1}$, where the last phase term arises due to a shift t_1 in the time domain. $e_i(\omega)$ is the real electric field envelope. The spectral phase is given by $\phi_i(\omega)$. The orientationally averaged fluorescence signal $\left\langle \psi_1^{(1)} \middle| \psi_2^{(1)} \right\rangle$ can then be expressed as

$$\left\langle \psi_1^{(1)} \middle| \psi_2^{(1)} \right\rangle = \frac{1}{3\hbar^2} e_1(\omega_{eg}) e_2(\omega_{eg}) |\hat{\mu}_{ge}|^2 e^{i\Delta\phi_{21}(\omega_{eg})} e^{i\omega_{eg} t_{21}}. \quad (1)$$

It is assumed that the signal is time-integrated by using a slow detector. In the semi-classical formulation of Heller and co-workers,[32] the above wave packet overlaps can be interpreted as an autocorrelation function of the excited state wavepacket $|\psi^{(1)}(t)\rangle$ such that the Fourier transform of this autocorrelation function can be directly related to the absorption cross section spectrally filtered by the excitation electric fields. Just like autocorrelation between first-order wavepackets depends on delay t_{21}, overlaps between nonlinear wavepackets, such as $\left\langle \psi_{124}^{(3)} \middle| \psi_3^{(1)} \right\rangle$ and $\left\langle \psi_{134}^{(3)} \middle| \psi_2^{(1)} \right\rangle$, are three-point autocorrelation functions and depend on time delays t_{21}, t_{32}, and t_{43}.

Equation (1) indicates that an optical frequency ω_{eg} is directly sampled as the time delay t_{21} is scanned. Furthermore, a spectrally imbalanced interferometer, for example, due to the spatial chirp in the acousto-optic modulator (AOM) diffracted pulse, imparts an extra phase $e^{i\Delta\phi_{21}(\omega)}$, which can distort absorptive spectral line shapes by mixing real and imaginary parts of the resulting spectra. In the AOPM approach, each pulse 1–4 is phase modulated by a radio frequency phase, $\vec{E}_i(\omega) = e_i(\omega)e^{i\omega t_i}e^{i\phi_i(\omega)}e^{i\Omega_i . nT_R}$, where T_R is the laser repetition rate and n denotes the nth laser shot. Thus, the carrier–envelope phase of each arm is dynamically phase cycled at a unique rate determined by the set radio frequency Ω_i. Taking this into account, the linear fluorescence signal becomes

$$\left\langle \psi_1^{(1)} \middle| \psi_2^{(1)} \right\rangle = \frac{1}{3\hbar^2} e_1(\omega_{eg}) e_2(\omega_{eg}) |\hat{\mu}_{ge}|^2 e^{i\Delta\phi_{21}(\omega_{eg})} e^{i\omega_{eg} t_{21}} e^{i\Omega_{21} . nT_R}, \quad (2)$$

with phase modulation in individual arms leading to an amplitude modulated signal at frequency Ω_{21}. This modulation frequency uniquely distinguishes the linear fluorescence signal arising from two different electric field interactions, against those that arise from the same electric field. Additionally, a reference signal is generated by passing the interfering electric fields through a monochromator set at a frequency ω_M. The resulting field autocorrelation signal is given by

$$R(\omega_M, t_{21}) = e_{R1}(\omega_M) e_{R2}(\omega_M) e^{i\Delta\phi_{R21}(\omega_M)} e^{i\omega_M t_{21}} e^{i\Omega_{21} . nT_R}. \quad (3)$$

The spectral phase difference $\Delta\phi_{R21}(\omega_M)$ between the reference electric fields after passing through the monochromator can be assumed to be negligible. The AOPM approach relies on detecting the wavepacket autocorrelation signal [Eq. (2)] relative to the optically generated reference [Eq. (3)]. The resulting demodulated lock-in signal, including the in-phase and in-quadrature components, now modulates as $Z(t_{21}) \sim e^{i(\omega_{eg}-\omega_M)t_{21}} e^{i\Delta\phi_{21}(\omega_{eg})}$. Note that the imbalanced spectral phase in the interfering electric fields will mix the absorptive and dispersive line shapes resulting from Fourier transform along t_{21}. Crucially, the optical frequency ω_{eg} is now undersampled at $(\omega_{eg}-\omega_M)$ imparting passive phase stability against fluctuations δt_{21} in the delay line. In the case of non-linear WPI, four-wavemixing signal pathways, such as rephasing and non-rephasing signals, can be isolated based on unique radio frequency combinations, $\Omega_- = (-\Omega_1 + \Omega_2) + (\Omega_3 - \Omega_4)$ and $\Omega_+ = (\Omega_1 - \Omega_2) + (\Omega_3 - \Omega_4)$, for rephasing and non-rephasing signals, respectively. Similar to physical undersampling of linear signals, optical coherences along the first and third time intervals, t_{21} and t_{43}, are undersampled as $(\omega_{eg}-\omega_{R1})$ and $(\omega_{eg}-\omega_{R2})$, respectively, where $\omega_{R1,2}$ are reference optical frequencies set by the respective interferometer. Note that the four wavemixing signal line shapes can also be distorted due to the imbalanced spectral phase $\mp\Delta\phi_{21}(\omega_{eg}) + \Delta\phi_{34}(\omega_{eg})$.

B. Experimental setup

The schematic of the fMES experimental setup is shown in Fig. 1 and implements the AOPM approach first demonstrated by Marcus *et al.*[13] Approximately 1 μJ, 300 fs pulses centered at 1040 nm from a 1 MHz Yb:KGW amplifier are focused into a 8 mm thick YAG crystal for the generation of white light continuum (WLC). The WLC is then routed to two pairs of chirped mirrors (CMs, Layertec 146851) for dispersion precompensation. A total of 34 pairs of bounces precompensates the expected optical dispersion in the setup. The pulses are then split by using a 50:50 broadband dielectric beam splitter (BS, Newport, 10Q20BS.1), and each portion routed to two different balanced Mach–Zehnder (MZ) interferometers, MZ1 and MZ2. Within each MZ, the time-delayed replicas are tagged with

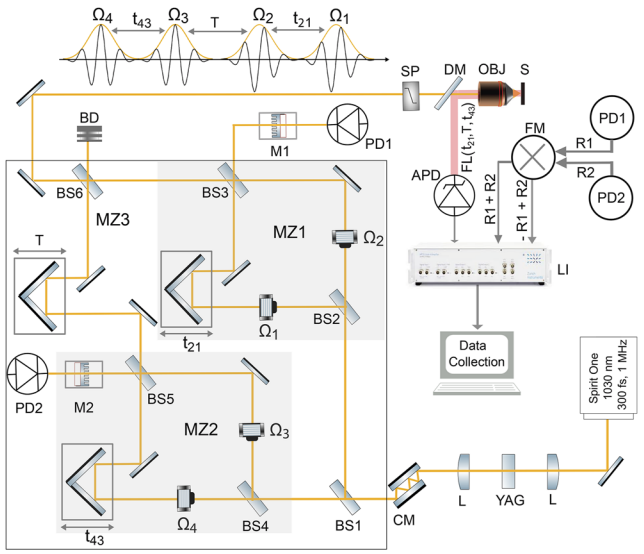

FIG. 1. Experimental schematic of the fMES spectrometer. Lens (L), chirped mirror (CM), beam splitter (BS), acousto-optic modulator radio frequency (Ω_s), Mach–Zehnder (MZ) interferometer, monochromator (M), photodiode (PD), beam dump (BD), shortpass (SP) optical filter, longpass dichroic mirror (DM), reflective objective (OBJ), sample (S), avalanche photodiode (APD), frequency mixer (FM), electronic reference (R1 and R2) and fluorescence (FL) signals, and lock-in (LI) amplifier. The experimentally controllable positive time delays (t_{21}, T, t_{43}) between the pulses are shown.

a unique carrier–envelope phase, which is cycled at radio frequencies using acousto-optic modulators (AOMs, I-M080-2.5C10B23-4-GH85, Gooch and Housego). The phase modulation frequencies of the four arms are phase-synchronized by controlling them through a common clock (Novatech 409B) and denoted as $\Omega_{i=1-4}$ in accordance with the pulse labels 1–4. The time ordering of the pulses is also shown in Fig. 1 along with the corresponding time intervals t_{21}, t_{32} or T, and t_{43}. When the split pulses within each interferometer, MZ1 and MZ2, are recombined at BS3 and BS5, respectively, the resulting pulse amplitudes modulate at the AOM difference frequencies Ω_{12} and Ω_{34} for MZ1 and MZ2, respectively. Ω_{ij} is defined as $\Omega_{ij} = \Omega_i - \Omega_j$. Pulse pairs from each MZ are recombined at BS6 to form the third MZ interferometer such that a collinear pulse train of four pulses, each with a unique carrier–envelope phase-shift, originates from BS6 for every laser shot. All time delays between the collinear pulses resulting after BS6 are controlled by translation stages (Newport MFA-CC for $t_{21,43}$ and Newport ILS150CC for T using the Newport ESP301 stage controller).

As shown in Fig. 1, one of the two output ports of each MZ is sent through a monochromator. The resulting output pulse of ~1 nm width is centered at $\lambda_{R1,2}$ = 635 nm and corresponds to a full-width at half maximum (FWHM) time envelope of ~0.6 ps. This ensures an approximately constant reference amplitude as t_{21} and t_{43} time delays are scanned. Before the pulse pairs from MZ1 and MZ2 are recombined, MZ2 (or probe) pulses are both time-delayed by a waiting time T. The collinear train of four pulses is passed through a 675 nm shortpass filter (SP, Edmund Optics) and a 660 nm longpass dichroic filter (DM, Edmund Optics), which reflects the laser spectrum toward the objective. The reflected spectrum is focused onto the sample using a (reverse Cassegrain) reflective microscope objective (Thorlabs, LMM-40X-P01, NA = 0.5). The fluorescence collection efficiency of this 0.5 NA microscope objective including the obscuration is ~5%. The sample is circulated through a 100 μm pathlength flow cell (Starna) using a peristaltic pump (Masterflex) with a sample flow rate of ~85 ml/min. Sample stability over the entire data collection time was ensured by comparing optical density (OD) and shape of the absorption spectrum before and after the experiment (Sec. S4). The amplitude modulated fluorescence resulting from the sample, with frequencies Ω_- and Ω_+ for rephasing and non-rephasing signal pathways, respectively, is collected in the confocal geometry, transmitted through a 700 nm long pass filter (Edmund Optics), and detected using an avalanche photodiode (APD, Hamamatsu C12703). The APD output is sent into a lock-in amplifier (Zurich Instruments, HF2LI) for phase-sensitive detection relative to optically generated reference signals.

The optically generated reference signals ω_{R1} and ω_{R2} modulating at frequencies Ω_{12} and Ω_{34} are digitized and mixed using a 24-bit audio signal processor (Analog Devices) to generate mixed reference signals modulating at frequencies $\Omega_\pm$. The mixed reference signals are connected as external references to the lock-in amplifier, and the rephasing and non-rephasing signals are detected in parallel channels using these references. As described in Sec. II A, such a detection scheme leads to physical undersampling of the optical frequencies at a shifted frequency $\omega_{eg}-\omega_R$ such that time intervals sampling optical coherences, t_{21} and t_{43}, are less susceptible to mechanical fluctuations and optical coherences can be undersampled. In the experiments, the AOM frequencies are set at Ω_1 = 80.109 MHz, Ω_2 = 80.107 MHz, Ω_3 = 80.005 MHz, and Ω_4 = 80.0 MHz through a common clock such that non-rephasing and rephasing 2D signals oscillate at 7 kHz (Ω_+) and 3 kHz (Ω_-), respectively. Modulation of the resulting nonlinear signal at kHz frequencies partly minimizes the $1/f$ noise. The powers per arm in each of the MZs are balanced by appropriately setting the AOM amplitudes so that on top of the microscope, we get an average power of 30 μW (corresponding pulse energy of 30 pJ) per interferometer.

The laser spectrum measured at the sample position is shown in Fig. 2(a) (gray shaded area). Shaping the generated WLC using optical filters in a confocal geometry simplifies spectrum generation but at the expense of a sloped laser spectrum with a sharp cutoff, as in our case. Such a spectrum will attenuate blue (high frequency) features in the 2D spectrum and the corresponding CM peaks such that not all CM peaks are expected to be equally intense. When quantitative 2D line shape analysis[33] is desirable, the frequency filter effect of the laser spectrum can be compensated by division, however, at the expense of increased noise in regions where the laser spectrum is sloped or of lower intensity.

Widely employed pulse characterization methods, such as frequency-resolved optical gating (FROG)[34,35] and multiphoton intrapulse interference phase scan (MIIPS),[36] rely on second-harmonic generation (SHG), where sufficient signal-to-noise ratio (SNR) and SHG bandwidth are for key reliability of pulse compression. In the current case of WLC-based fMES, this becomes challenging not only due to pJ pulse energies but also due to the experimentally challenging collection of the broadband UV spectrum through a microscope objective typically designed for the visible or near-infrared. On the other hand, a wide variety of materials that exhibit two-photon-induced photocurrent have been shown to yield reliable results,[37,38] with maximum peak intensity attained for a transform-limited pulse. To measure the pulse duration, we used a pair of pulses from an interferometer and focus on a silicon carbide two-photon photodiode (SiC, Boston Electronics sg01XL-5ISO90) using the reflective microscope objective (OBJ) to record the two-photon autocorrelation signal. The diode was chosen so as to ensure that the spectral responsivity curve overlaps well with the expected second harmonic of the laser spectrum. The resulting interferometric autocorrelation is shown in Fig. 2(b). By Fourier transforming the autocorrelation trace and numerically filtering out the oscillating components, we obtain a pulse duration of ~13 fs at the sample position [Fig. 2(b), inset]. Note that interferometric autocorrelation does not characterize the spectral phase. In a highly dispersive setup, such as here, pulse compression using chirped mirror pairs may nearly compensate for second order dispersion. However, significant third order dispersion is still expected to introduce distortions in the interferometric autocorrelation, such as increased amplitude in the wings. Measurements of a vibrational quantum beat of half period ~28 fs, presented in Sec. III C, suggest that residual phase distortions do not significantly affect coherent excitation of such a beat. We also simulated the autocorrelation trace from the measured laser spectrum [gray shaded area of Fig. 2(a)], assuming a transform-limited pulse. From the simulated trace, the obtained pulse duration is ~12 fs (Fig. S2). This corresponds to ~21 fs^2 uncompensated second order dispersion, which can stretch the pulse duration from 12 to 13 fs. The pronounced wings in the autocorrelation trace, observed in both the measured and simulated traces, are explained by the sharp cutoff introduced by optical filters and

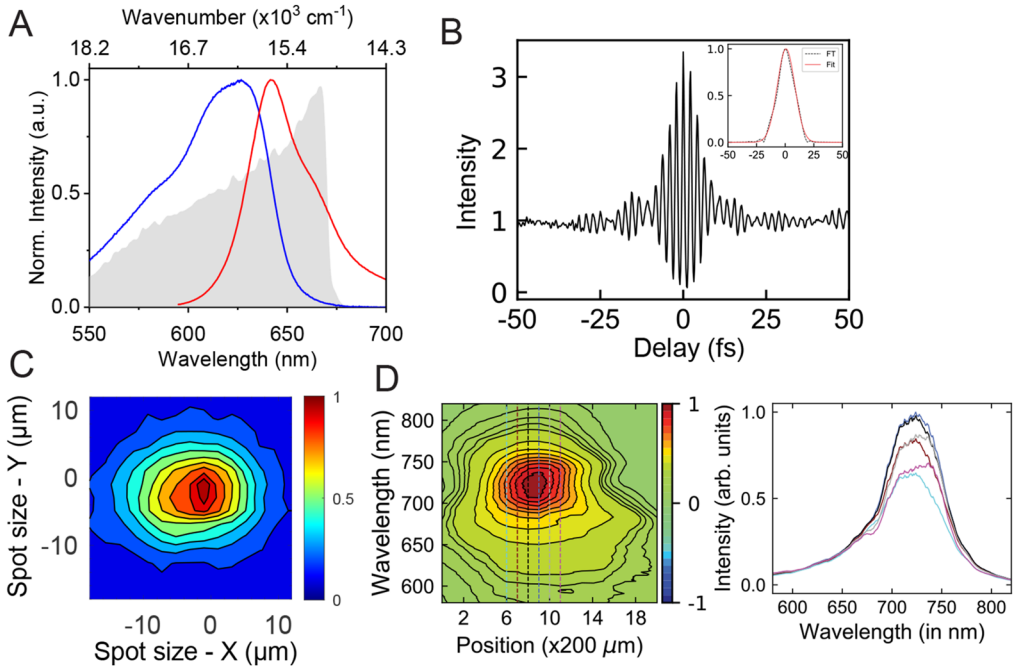

FIG. 2. Pulse characterization. (a) Linear absorption (blue) and fluorescence (red) spectrum of oxazine in ethanol, overlaid with the measured laser spectrum (gray shaded area). (b) Experimentally measured collinear interferometric autocorrelation (IAC) trace (black) by placing a two-photon SiC photodiode at the objective focus. Fourier filtered trace of the IAC and fitted with an assumed Gaussian pulse (red, inset), which shows a FWHM pulse duration of ~13 fs at the sample position. (c) Spot profile measured at the sample position using a monochrome CMOS sensor. Contours are drawn at the 5% and 10%–100% in 10% intervals. The raw image is shown in Fig. S1(A). A 2D elliptical Gaussian fit yields FWHM spot sizes of ~14, 11 μm. The detailed description of the spot size measurement is given in Sec. S1. (d) Spatial chirp measurement. Normalized contour plot of the laser spectrum collected in 200 μm intervals horizontally across the spot transverse profile before the shortpass filter. Contours are drawn at the 5% and 10%–100% in 10% intervals for positive or negative contours. Dashed vertical lines are drawn within 60% of the maximum amplitude in the spot transverse profile. Vertical slices at marked positions are plotted (right panel) to show the variation of the spectrum over the transverse profile.

uncompensated higher-order dispersion. We could not reproduce the expected 8:1 ratio in the autocorrelation. Experimental measurement of MZ modulation depth (MD) and simulations of interferometric autocorrelation suggest that imperfect MD (~80%), likely arising due to the spatial mode mismatch in the interferometer and residual angular dispersion and spatial chirp at the objective focus, can partly account for this reduced ratio. Measurement of a short DC component of interferometric autocorrelation at the objective focus suggests that such imperfections are likely not significant compared to focal spot size. Details of interferometer MD measurement and corresponding simulations are presented in Sec. S8.

The spot size was characterized at the focus position after the reverse Cassegrain reflective objective and is shown in Fig. 2(c). The spot was measured by scanning a monochrome CMOS sensor (pixel resolution 2.08 × 1.95 μm^2) across the focus. The average FWHM focal spot size is ~12 μm. Note that much smaller spot sizes could be obtained using glass objectives at the cost of excessive optical dispersion or with reflective objective but at the cost of obscuring the core of the beam leading to insufficient pulse energies. Residual angular dispersion and spatial chirp are expected in broadband setups relying on AOMs, such as the AOPM approach implemented here. Spatial filtering and AOM double-passing[39] have been suggested[27] to compensate for angular dispersion and spatial chirp almost exactly although at the cost of introducing optical dispersion and high power loss in the AOMs. Another way to minimize angular dispersion with lesser amount of extra optical dispersion and minimal extra power loss is through the use of lenses immediately after the AOM in order to prevent angular dispersion in the beam travel path. A collimation lens immediately after the AOM converts the angular dispersion into a spatial chirp. We used a 40 cm lens to softly focus into the AOMs and a 30 cm lens after the second beam splitter of the MZ for collimation. We choose the focusing lens such that the Rayleigh range over which the spot doubles is larger than the AOM crystal length. The collimation lens focal length is determined by how close it can be kept to the AOMs. Note that the beam splitters after the AOM will also introduce further angular dispersion. The collimation lens compensates for angular dispersion introduced by the AOMs and the beam splitter after the AOMs (BS3,5) by converting it into spatial chirp. However, the final beam splitter of the setup (BS6) is also expected to introduce some amount of angular dispersion, which is not compensated. We have characterized the spatial chirp in the transverse spot profile before routing it through the shortpass and dichroic filters and the objective. This is shown in Fig. 2(d). The spot profile is ~1.6 mm in diameter, and the full spectrum at each point of the profile is measured by scanning a fiber of core diameter 200 μm (Thorlabs, M25L01) across this profile. The

fiber coupler was placed on a mechanical translation stage (Thorlabs, PT1, least count 20 μm), and the spectrum was taken at every 200 μm interval. The spatial chirp at the focus, compared to 12 μm focal spot size, is further minimized through achromatic focusing from a reflective objective. Minimization of spatial chirp is expected to reduce any spectral phase imbalance in the MZ interferometers such that the imaginary component in the fluorescence excitation spectrum should be minimized. We confirm this further in Sec. II E. In the case of sub-micron focal spot sizes, a direct measure of spatial chirp could be done using plasmonic nanoparticles at the focus.[40]

C. Data collection scheme

Construction of the fMES dataset requires signal collection at each time delay along the delay axes (t_{21}, T, t_{43}). Even though noisy data points near zero delay affect the signal the most, typically delay scans, at a fixed T, have been done[8] by sampling the optical coherence axes (corresponding to delays t_{21} and t_{43}) as a uniform (t_{21}, t_{43}) grid through either stepwise or continuous stage scanning[18] or through a pulse shaper.[9] In our case, the central motivation is to minimize sample exposure and simultaneously ensure that the T axis is least susceptible to laser drifts. When unexpected experimental interruptions are expected, the "quadratic sampling" scheme has been suggested[41] in the context of the SLM-based phase cycling approach to fMES. Figure 3(a) explains the alternative data collection scheme employed here. Stepwise sampling along the optical coherence axes (t_{21}, t_{43}) is biased toward the sampling delay points with equivalent time delays, rather than as a uniform raster scanned grid. This is shown in Fig. 3(a), where data points of the darker shade are scanned first and data points of the same shade are scanned consecutively. With this scheme, the data points at which the signal S(t_{21}, t_{43}) is expected to be the weakest are scanned at the very end, thus making the measurement less susceptible to long-term laser drifts. Note that the combination of biased sampling and rapid T scanning presented here is advantageous when (t_{21}, t_{43}) grid is small, that is, for samples with fast optical dephasing. However, for samples with optical linewidths[26,28] of only a few meV, the rapid scan of (t_{21}, t_{43}) delays[18,26] for a given T may amount to higher experimental throughput when T dynamics is not the key feature of interest.

Following the above biased sampling scheme, the time delays are scanned stepwise from 0 to 51 fs in steps of 3 fs, which corresponds to a Nyquist frequency of ~5556 cm^{-1}. The signal level at $t_{21,43}$ = 51 fs is already below 5% of the maximum signal, implying a system limited frequency resolution in the Fourier transformed 2D spectra. Another crucial departure from the existing sampling schemes is that the pump–probe delay (T) is scanned continuously from −50 fs to 1 ps with a uniform stage velocity of 20 μm/s, corresponding to the 7.5 secs/sweep/$t_{21,43}$ data point. This minimizes the continuous sample exposure window substantially compared to existing approaches to provide a scalable route toward spatially resolved measurements where reducing the sample exposure window becomes highly desirable. Signals are digitized at a sampling rate of 7.2 k samples/sec with a lock-in time constant of 5 ms and a 48 dB/oct filter. With an acceleration of 20 mm/s^2, the stage reaches the set constant velocity in a distance of the order of minimum incremental resolution of the stage. Scanning from −50 fs allows us to accurately determine the zero T index by averaging multiple

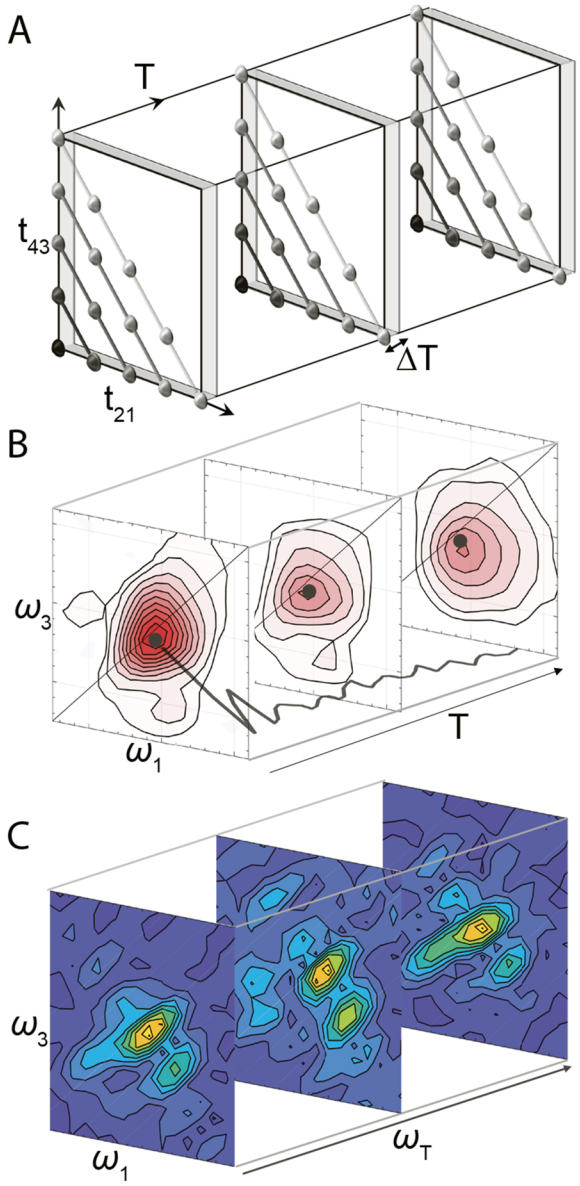

FIG. 3. (a) Schematic for data collection and processing methodology. t_{21} and t_{43} points (shaded dots) are scanned step-wise, with points of same shading scanned consecutively. For each ($t_{21,43}$) point, the pump–probe delay T is scanned continuously at a constant velocity. Multiple sweeps along T scans are averaged first, followed by binning of averaged ($t_{21,43}$) data points into ΔT intervals. (b) For each pump–probe delay T, Fourier transforms along (t_{43}, t_{21}) yield a correlated map of detection vs excitation frequency. Each pixel of the 2D spectra in the resulting 3D dataset, depicted as the gray oscillatory line, thus, corresponds to a continuous T scan. (c) The pixels are fitted globally with a tri-exponential rate model to remove the exponential decay background, followed by the Fourier transform of the residuals to obtain coherence maps along the ω_T coherence axis.

$t_{21,43}$ sweeps. This is described in Sec. II E. The continuous T axis is then constructed using the T zero index, lock-in sampling rate, and stage velocity. The constructed T axis and whether the combination of lock-in time constant, filter, and stage velocity can adequately

reconstruct T signal kinetics were double checked by overlaying *step* scans along T for a fixed (t_{21}, t_{43}) delay with *continuous* T scans (Secs. S5 and S6).

In the above scheme, the stage velocity and lock-in settings (time constant τ_{LI} and filter roll-off) together determine the binned time step (Sec. II D) in the experiment. For example, our choice of velocity (20 μm/s) and τ_{LI} settings (5 ms, 48 dB/oct filter) is such that the time it takes for the stage to scan a delay of 10 fs corresponds to the signal settling to >99% of the actual value. Total 4 sweeps along the increasing T direction are averaged. A slower lock-in time constant or a faster velocity makes T resolution poorer although the latter also makes the experiment faster and could be done to further optimize the experiment and minimize the sample exposure window. See Sec. S5 for further details.

With the above scheme, the collection of one full 3D dataset takes ~40 min with one T sweep per (t_{21}, t_{43}). For the 2DES data reported in Sec. III, total 4 T sweeps per (t_{21}, t_{43}) are performed. In comparison, stepwise scans along T at a 1 MHz repetition rate, with substantially poorer SNR compared to 83 MHz,[15] would have taken ~1.5 h for one T scan, assuming the same time resolution, scan range, and stage wait time of 150 ms (lock-in time constant of 30 ms). Due to the long data collection times with the T axis being the slowest, step scanning T makes the measurement of weak coherences along T most susceptible to laser drifts. In the case of continuous T scanning, reduced data collection time and, therefore, less susceptibility to laser drifts, multiple sweeps along T, and the ability to bin multiple T samples to get a well averaged $t_{21,43}$ data point (Sec. II D) are expected to contribute to higher SNR. Fine sampling along T has also been suggested[5,42,43] to effectively average out high-frequency noise in the data.

D. Data processing

As shown in Fig. 3(a), multiple sweeps along T are averaged first, followed by binning of averaged T sweep into intervals ΔT = 10 fs. For a 10 fs step size, a total of ~540 samples fall within each T bin as determined by the sampling rate and stage velocity. These data points are averaged together to form one $t_{21,43}$ averaged data point. Overall, the averaging and binning procedure yields a 3D grid of 18 × 18 × 101 time points along t_{21}, t_{43}, and T delay axes, respectively.

In the AOPM approach implemented here, simultaneous collection of both rephasing and non-rephasing signals, modulating at unique modulation frequencies, Ω_- and Ω_+, respectively, is possible through two parallel lock-in channels referenced to corresponding optically generated and digitally mixed frequencies. At each pump–probe waiting time T, the data are zero-padded up to 64 grid points, prior to the Fourier transform along t_{21} and t_{43}. Note that zero-padding up to 2 × 18 number of points is allowed[44] by Kramer–Kronig relations and yields a frequency resolution of ~327 cm^{-1} along the corresponding $\omega_{1,3}$ axes. Increasing the number of points from 36 to 64 (nearest power of 2) interpolates the data without enhancing spectral resolution, which is system limited due to fast optical dephasing within ~50 fs. The 2D Fourier transform of the complex dataset yields a correlated map of detection frequency (Fourier transform of t_{43} to ω_3) vs excitation frequency (Fourier transform of t_{21} to ω_1) for a given T. Rephasing and non-rephasing spectra are phased separately and added in the frequency domain to yield an absorptive 2D spectrum. The phasing procedure is discussed in Sec. II E.

As depicted in Fig. 3(b), a given pixel in the 2D plot may have contributions from coherent and incoherent signal pathways along T. For isolating the coherences in the collected data, the 3D rephasing dataset is fit globally to a tri-exponential fit, which removes incoherent exponentially decaying population signals from the data. The 3D dataset can be fit from T = 0 fs because the elimination of non-resonant signals and scatter in fluorescence-detection make early T signals easily accessible in fMES. The resulting residuals are zero padded from 101 to 256 points along T prior to the Fourier transform although the expected frequency resolution of ~16.5 cm^{-1} along ω_T corresponds to only twice the range scanned along T. This results in a three-dimensional frequency cube $S(\omega_1, \omega_T, \omega_3)$, shown in Fig. 3(c) with coherence frequency $\pm\omega_T$ corresponding to T. The total ω_T frequency content in the data is given by the Frobenius norm defined as $F(\omega_T) = \left|\sqrt{\sum_{i,j}|S(\omega_{1,i}, \omega_T, \omega_{3,j})|^2}\right|$. $F(\omega_T)$ reports on the most prominent frequencies in the dataset and the noise floor of the collected data. For a given coherence frequency ω_T, plotting the absolute value of the Fourier transformed signal as $|S(\omega_\tau, \omega_t; \omega_T)|$ is referred to as a coherence or beating map at ω_T and reports 2D positions of the most prominent quantum beating amplitudes. With sufficient experimental SNR and phase stability, further separation of coherent signal pathways contributing to CMs is possible by starting from the complex rephasing dataset. The resulting sign of the coherence frequency, $\pm\omega_T$, is physically significant and can be used to isolate various ground and excited state quantum beat pathways.[45] This is demonstrated in Sec. III.

E. Determination of zero delays and phasing

The zero time delays for t_{21} and t_{43} optical coherence axes are determined by collecting the linear fluorescence signal separately for each interferometer MZ1 and MZ2, where the signals are modulated at the difference AOM frequencies Ω_{12} and Ω_{34}, respectively. The respective zero time delay for an interferometer is determined by the maximum absolute value of the demodulated linear signal by scanning the respective delay from −60 to +60 fs in 1 fs steps, with the stage settling time of 200 ms (greater than 5 times the lock-in time constant). Multiple trials are repeated to determine an average zero time delay position along each delay axis with an error bar of ~0.2 fs, which is within the minimum incremental delay resolution (0.7 fs) possible with the stage. The T zero delay is obtained by scanning the fixed arm of each interferometer (arms 2 and 3) with modulation frequency Ω_{23}. Other combinations, for example, between arms 1-4 and 1-3 and 2-4, were also verified to yield the same zero T delay. Since the T delay is scanned continuously during 3D dataset collection, the zero delay position obtained above is only a reference time point for phasing the lock-in signal, while the T zero delay point needs to be re-determined for the continuous scan. As discussed in Sec. II C, continuous scans from −50 fs for each grid point (t_{21}, t_{43}) can be overlaid to determine an average T = 0 fs position. However, fast optical dephasing along $t_{21,43}$ implies that this can be reliably done only for the first few time delay points [darker shades in Fig. 3(a)]. This is discussed in Secs. S5 and S6.

Spectral phase imbalance in the interferometer, for example, due to the spatial chirp, can lead to residual phase $\mp\Delta\phi_{21}(\omega_1) + \Delta\phi_{34}(\omega_3)$ in the rephasing and non-rephasing signals (Sec. II A). The residual phase mixes the real and imaginary line shapes to yield mixed absorptive and dispersive line shapes in the absorptive 2D spectra. In the case of time-domain fMES implementation discussed here, interferometer drifts or zero-delay errors in MZ1 and MZ2, denoted as $\delta t_{21,34}$, cause phase drifts $\mp\Delta\omega_1\delta t_{21} + \Delta\omega_2\delta t_{34}$ in rephasing and non-rephasing signals, respectively. Here, $\Delta\omega_{1,2}$ is defined as $\omega_{eg}-\omega_{R1,2}$. The resulting phase drifts also mix real and imaginary line shapes in the individual channels.

In conventional MES, the total residual spectral phase is approximated as $\Delta\phi(\omega) = \phi_o + \omega\delta t + \phi''\omega^2/2$ and can be corrected in the frequency domain along the detection axis, assuming no residual phase along the excitation axis. In the AOPM approach, contributions from both $\Delta\phi_{21}(\omega_1)$ and $\Delta\phi_{34}(\omega_3)$ are expected. The arbitrary constant phase due to lock-in detection is set to zero at the start of the experiment, while $\omega_{R1,2}$ can be chosen to minimize phase drift contributions. In order to correct fMES spectra for interferometer imbalance arising from a spatial chirp, Agathangelou *et al.* derived[18] the residual spectral phase, $\Delta\phi_{21}(\omega)$ and $\Delta\phi_{34}(\omega)$, by collecting the linear fluorescence signals from MZ1 and MZ2 [Eq. (2) of Sec. II A], respectively. A symmetrically scanned linear fluorescence signal is expected to be completely real; hence, a substantial relative magnitude of the imaginary part would indicate a spectral imbalance within the interferometer, which can then be corrected. In our approach, constant phase factors $\phi_o^{R,NR}$ that mix real and imaginary parts of rephasing and non-rephasing channels phase the absorptive 2D spectra fairly well for all T, better than <5% imaginary components measured from linear excitation spectra (Fig. S6) and field autocorrelation (Fig. S7). This is shown in Fig. S6 where the residual spectral phase derived from the linear signal is found to be insufficient to correctly phase the 2D spectrum. Uncertainty in phase characterization of the order of 5% may easily arise because the particular way of grid scanning introduced here does not allow us to track real-time interferometer drifts.[18,26] Instead, the phase is characterized prior to the 2D scans and does not account for such drifts.

III. RESULTS AND DISCUSSION

In this section, we discuss the sensitivity of fMES followed by an experimental demonstration, which serves as a measure of sensitivity. Following the approach described in Sec. II C, high SNR detection of 2D spectra down to 2–3 orders of magnitude lower OD than typical approaches is presented. This is extended one step further to demonstrate phase-sensitive detection of vibrational quantum beats in the form of 2D CMs of a laser dye oxazine 720 in ethanol at room temperature. The sample preparation at different concentrations, linear absorption, and fluorescence spectra of oxazine 720 in ethanol are described in Sec. S3.

A. Sensitivity of fMES

In the context of pump–probe measurements, Cho *et al.* derived and experimentally verified[46,47] expressions for absolute photon number changes in the probe beam caused by the pump. These expressions are consistent with the expression[48] for the relaxed 2D spectrum incorporating propagation distortions caused by the attenuation of excitation pulses and the signal as they travel through a sample and serve as a useful starting point to think about the dependence of the fMES signal on the experimental parameters. The non-linear fluorescence signal S_f for a two-electronic level system can be simply expressed as

$$S_f \sim f_{rep}\Phi[\rho_u(x,y,z)\delta.N_o\sigma_{ge}L][\rho_r(x,y,z)\delta(\sigma_{ge}+\sigma_{eg})]\eta_{\text{det}}. \quad (4)$$

In the above equation, f_{rep} is the repetition rate; Φ is the quantum yield, which is assumed to be excitation frequency-independent; N_o is the molecular number density in the ground electronic state; and L is the sample pathlength. Polarization and T lifetime dependence have been ignored. The simplified equation [Eq. (4)] assumes approximately transparent samples with no fluorescence reabsorption, identical pump pulses, and identical probe pulses. Pump and probe pulses are denoted by subscript "u" and "r," respectively. The pump and probe spectrum is assumed to be nearly monochromatic with width δ. As in Ref. 47, the first term in the square brackets arises from the total number of molecules excited by the pump as it travels through the sample. The term in the second square bracket arises from the overlap of probe pulse spectrum with the absorption and emission cross sections. Although the pump and probe are always fully overlapped in a collinear geometry, an additional assumption in Eq. (4) is that of constant pump and probe spot sizes within the sample pathlength such that the entire pathlength L contributes to the signal. This assumption does not hold when focusing using a microscope objective and only a smaller region within L where the fluence is maximum dominantly contributes to the nonlinear signal. For example, the authors of Ref. 15 discussed that the majority of the non-linear signal along the axial direction is generated from within the point spread function (PSF) created by the objective. This can also be incorporated explicitly in the fluence $\rho(x,y,z)$ by including the transverse profile dependence as the beams contract, focus, and expand within the 100 μm sample pathlength. However, we have checked the validity of the above assumption. This is shown in Fig. S1. The last factor η_{det} in Eq. (4) represents the overall loss of the time-integrated fluorescence signal in the detection line, which includes the overlap of the longpass optical filter with the steady-state fluorescence spectrum of the sample, fluorescence collection efficiency of the objective, and spectral responsivity and gain of the APD. White noise and pink $(1/f)$ noise can be minimized through a lock-in frequency filter and averaging and phase-modulation at high frequencies, respectively. The noise in data collection at a given modulation frequency also depends on how the APD gain-dependent noise spectral density[49] compares with the signal size S_f. All such noise contributions together determine the signal-to-noise ratio (SNR) of the experiment. Overall, Eq. (4) indicates that $S_f \approx \sigma OD$ and that a fair comparison of experimental sensitivity must ensure that f_{rep}, Φ, η_{det}, fluence ρ, and absorption cross section σ are comparable. Note that the fluence per pulse used in our experiment is ~12 μJ/cm^2, corresponding to a pump excitation probability[46] of <1% at the center of the beam profile.

With above considerations, the signal size is expected to be proportional to OD for ODs $\ll 1$. Conventional 2DES measurements have been conducted at an OD of ~0.3 where the four wavemixing

signal maximizes.[46,48] Hence, as a first demonstration of the continuous T scanning approach to fMES, we present the absorptive 2DES spectra at ODs ~2–3 orders of magnitude lower than what is typical.

B. 2D spectra vs sample OD

Oxazine 720 (also known as Oxazine 170) is a laser dye in the oxazine family commonly used as a near-IR fluorescent probe for bio-imaging applications. Oxazines are derived from xanthenes by replacing the central carbon with a nitrogen atom, which, unlike the central carbon, participates in π-conjugation, resulting in an ~100 nm red-shift of the $S_0 \rightarrow S_1$ transition. Oxazine 720 has a fluorescence quantum yield[50] of ~0.53 in ethanol with absorption and fluorescence peaks located at 627 and 641 nm, respectively [Fig. 2(a)]. The blue shoulder in the absorption spectrum is expected to be a Franck–Condon (FC) progression.[51] Oxazine 720 is also known to exhibit solvatochromism, with Stokes' shift increasing with solvent polarity. In polar solvents, such as methanol, the ion-pair in oxazine 720 breaks and the cationic skeleton is expected to be less rigid although Condon approximation seems to hold.[52] It is reported[53] that upon photoexcitation, the permanent dipole moment of oxazine 720 increases substantially in the excited state. The author of Ref. 51 also reported the increased strength of solute–solvent H-bonding upon electronic excitation. Thus, rich photoinduced solvation dynamics is expected for this laser dye and will be a subject of future investigations in our group. Figure 4 shows the experimentally measured absorptive fMES 2D spectra for representative pump–probe delays T = 0, 100, 1000 fs. The three rows in Fig. 4 compare the room temperature 2D spectra at three different sample ODs ranging from ~1 to 100 mOD. In terms of experimental parameters, the three datasets only differ in terms of sample OD and the APD gain, ignoring the day to day variations in experimental conditions. Rich solvation dynamics is evident in the 2D spectra with the rapid loss of frequency correlation and red-shifted detection frequency (Stokes' shift) seen within ~1 ps. The 2D spectra and features associated with solvation dynamics are consistent to within ~10% contour across the range of ODs measured, indicating the high-sensitivity of detection at ODs ~300× lower than what is typical in 2DES.

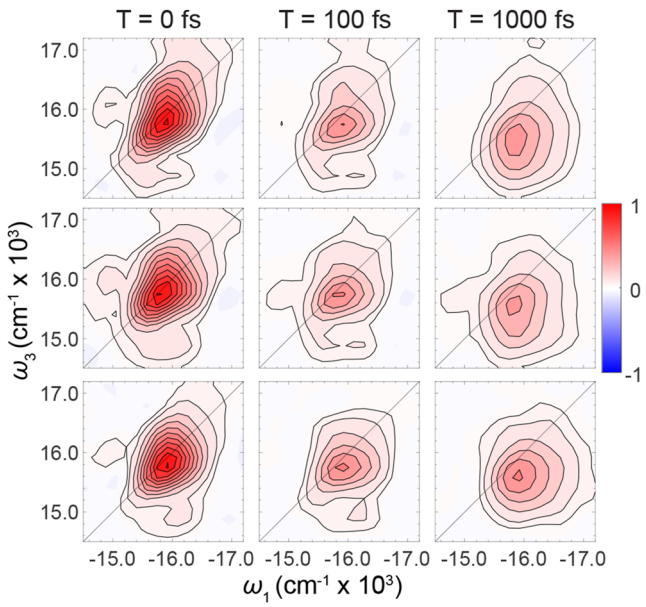

FIG. 4. Real absorptive two-dimensional electronic spectra of oxazine 720 in ethanol in a 100 μm pathlength flow cell at the pump–probe waiting times T = 0 fs, T = 100 fs, and T = 1 ps. The sample OD is (top row) 96 mOD, (middle row) 9.5 mOD, and (bottom row) 1.4 mOD. Contours are drawn at the 5% and 10%–100% in 10% intervals for both positive or negative contours.

Starting with ~0.3–0.4 sample OD optimized[46,48] for a maximum signal size, pump–probe measurements have routinely reported signal amplitudes of ~10 mOD. An optimized pump–probe spectrometer with a parallel reference spectrograph and shot-to-shot detection has reported[21,54] noise baselines of the order of 1 mOD (10^{-3}). Compared to these earlier works, measurements of consistent 2D spectra and solvation dynamics reported here are significant because the *starting* sample OD is as low as ~1 mOD. Recently, Tokmakoff and co-workers have also reported 2DIR spectra at concentrations ~1/2 of typical, where the sensitivity enhancement is achieved by encoding mid-IR transitions as electronic excitations and detecting the resulting fluorescence.[17]

C. Coherence maps vs sample OD

Amplitude modulations resulting from intramolecular vibrational wavepackets at room temperature are typically only a few percent of the incoherent population. For example, a FC displacement of half the zero-point amplitude results in a 2D oscillation amplitude[55] of ~12.5% of the maximum 2D signal expected from a monomer. 2D CMs can isolate[56] excited state wavepackets based on a quantum beat phase along T. However, this requires high SNR detection of vibrational wavepackets at room temperature. This becomes especially challenging with a WLC based setup where 5% RMS spectral fluctuations across the entire spectral bandwidth are typical[22,54,57] compared to light sources based on multi-stage optical parametric amplifiers (OPAs) operating in the saturation regime.[58] Thus, a further demonstration of the sensitivity of fMES would be a measurement of CMs from weak vibrational wavepackets along with the quantum beat phase at the lowest sample ODs.

Conventional 2DES experiments[59,60] on the oxazine family of dyes have reported a prominent intramolecular Raman-active mode around ~586 cm^{-1}, associated with in-plane bending motion of the phenyl ring. Turner *et al.* also implicated[61] this mode as the coupling mode responsible for coherent surface crossing mediated by a conical intersection in the related laser dye cresyl violet. Their quantum-chemical computations[62] suggest that the prominent vibrational mode of ~586 cm^{-1} exhibits a much larger Huang–Rhys (HR) factor of ~0.28 than other modes present in the system. The 2DES vibrational wavepacket modulation from this HR factor is expected to be only ~1/3 of the incoherent population background. In comparison, for an acene family of molecules, such as pentacene, HR factors >1 are typical, leading to facile detection of dominant vibrational wavepackets at room temperature.[63]

Figure 5 compares real rephasing CMs and the associated SNR for measurements on oxazine 720 with sample ODs ranging from ~1 to 100 mOD. As mentioned in Sec. III B, only APD gain is changed

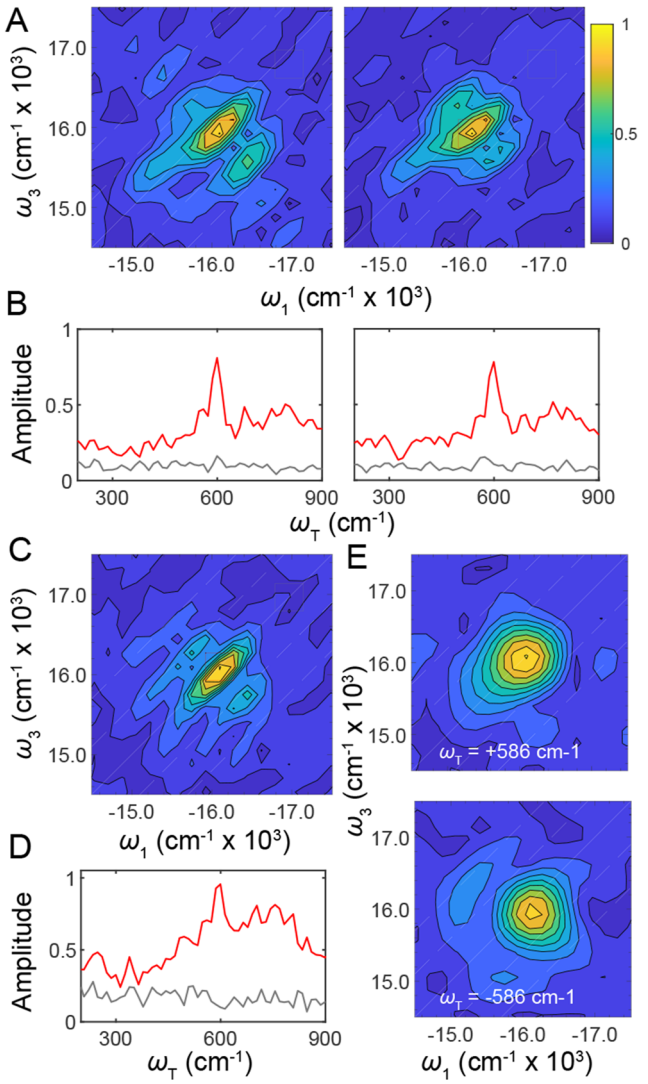

FIG. 5. (a) Real rephasing coherence maps (CMs) for ω_T = 586 cm^{-1} measured with a sample OD of 96 mOD (left) and 9.5 mOD (right). The diagonal line in the CMs corresponds to the 2D diagonal, and the dashed lines are separated by one quantum of ω_T vibration (586 cm^{-1}). Contours are drawn at the 5% and 10%–100% in 10% intervals. The CMs are normalized to their corresponding maxima. Red squares are drawn around the maximum amplitude of the map, and the gray squares are drawn at a position of almost two vibrational quanta away from the red squares. (b) Frobenius spectra are calculated over the above red (signal) and gray (noise) areas of (left) 96 mOD and (right) 9.5 mOD CMs. (c) Real rephasing CM for ω_T = 586 cm^{-1} measured with a sample OD of 1.4 mOD. The corresponding Frobenius spectra are shown in (d). (e) Complex rephasing CM $+\omega_T$ (top) and $-\omega_T$ (bottom) for the vibrational frequency of 586 cm^{-1} measured at a sample OD of 1.4 mOD. $\pm\omega_T$ maps are normalized with respect to the common maxima of two maps.

between the experiments, while the number of T averages is the same between the scans. The experimental CMs of the most prominent vibrational mode at ω_T = 586 cm^{-1} are shown in Fig. 5(a). The maximum CM amplitude for a given OD also corresponds to the maximum amplitude coordinate in the respective 2DES spectrum at T = 0 fs. We also observe that the maximum CM amplitude is ~ 1/4 of the maximum 2D amplitude (see Table S1). This suggests that the FC displacement of the 586 cm^{-1} mode may be smaller for oxazine 720 in ethanol than that for cresyl violet as reported by Turner *et al.*[62] The CM amplitude positions are approximately consistent with a displaced harmonic oscillator model of one vibrational frequency mode at 586 cm^{-1}.

As shown in Fig. 5(c), the CM features for the lowest sample OD (~1 mOD) are fairly consistent (to within ~20%) with those of the highest OD. Variations in the blue shoulder of the laser spectrum across different datasets can cause variations in the amplitude of off-diagonal higher frequency CM peaks. Figures 5(b) and 5(d) show the SNR analysis for each of the CMs collected across different sample ODs by evaluating the Frobenius norm over the main CM amplitude region and a noisy region where no CM amplitude is expected. Both regions are marked as squares in Fig. 5 and consistent across the three cases. It is seen that the SNR of ~8.5 for ~100 and ~10 mOD cases does not deteriorate, whereas for the case of ~1 mOD, the SNR deteriorates to ~5.5. The noise floor deterioration at the lowest sample OD may be expected due to a larger APD gain,[49] degrading the spectral noise floor.

In a real rephasing, CM vibrational wavepackets from both excited and ground states contribute at the diagonal peak such that the diagonal CM amplitude represents the sum of both pathways, which can be separated based on the quantum beat phase along ω_T.[64] Figure 5(e) isolates excited state contributions by plotting rephasing 2D CMs at $\pm\omega_T$ = 586 cm^{-1} for the lowest sample OD. The location of the peak positions can be explained[64] through Feynman pathways considering a displaced harmonic oscillator model such that $+\omega_T$ contributions are expected to arise only from the excited state vibrational quantum beats. Although the individual CM peak contributions are merged together, diagonal contributions seem more prominent compared to other 2D locations. The resulting $\pm\omega_T$ CMs suggest that an SNR of ~5.5 is good enough for isolating excited state $(+\omega_T)$ contributions with a respectable SNR. Overall, consistent CM measurements at ODs 2–3 orders of magnitude lesser than typical demonstrate the sensitivity limits of the approach implemented here. It should also be pointed out that even though the measurement sensitivity reported here is high enough to yield an SNR of 5.5 for the most prominent mode at ODs 2–3 orders of magnitude lower than typical, only one prominent mode is consistently seen in the experiments, suggesting overall sensitivity limitations in constructing the ω_T dimension despite T averaging.

More number of T sweeps is expected to improve the SNR for the case of ~1 mOD although at the cost of increased experimental time. Instead, a significantly faster experiment, similar to a spectrally resolved pump–probe (SRPP) experiment,[31] can be performed by fixing t_{21} = 0 fs. The rest of the parameters are exactly the same as in Sec. II C. A related fluorescence-detected pump–probe (fPP) experiment has been recently reported by Maly and Brixner.[65] Although excitation frequency information is not available in a pump–probe experiment, high-sensitivity detection of coherent wavepackets at the lowest ODs, collection of both rephasing and non-rephasing channels, and isolation of pathways based on a quantum beat phase are still possible in the AOPM approach to fPP, taking it beyond conventional pump–probe spectroscopy. A pump–probe delay T was

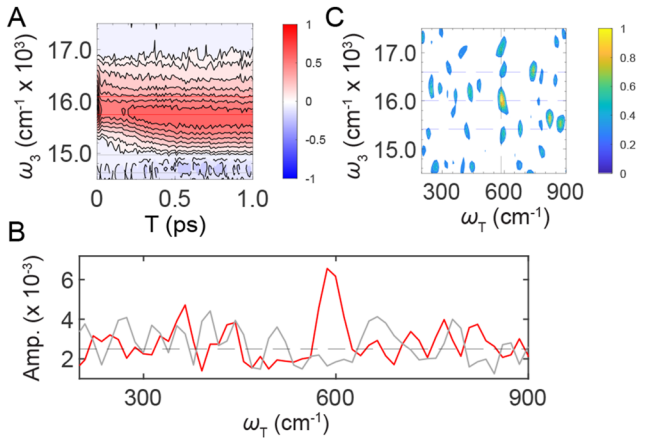

FIG. 6. (a) Normalized real rephasing spectrally resolved pump–probe (SRPP) data for a 1.4 mOD sample of oxazine 720 at room temperature averaged over 8 T sweeps. Contour lines are drawn at the 5% and 10%–100% in 10% intervals for both positive or negative contours. (b) Frobenius spectra were calculated over red and gray regions marked in (a). The prominent vibrational frequency at ω_T = 586 cm^{-1} was also seen in the 2D CMs. A horizontal dashed line is drawn at ~30% of the maxima value of the Frobenius spectrum to denote the average noise floor. (c) Normalized absolute squared Fourier transform map of the SRPP data obtained after a three-exponential global fit of the population kinetics. Here, the contours are drawn from 30% to 90% in steps of 10% and 90%–100% in 2% intervals. A vertical dashed line marked at ω_T = 586 cm^{-1} shows the prominent vibrational frequency. The central dashed horizontal line is drawn at a position corresponding to the 2D CM maximum, and the other two lines are drawn at one vibrational quantum above and below the main peak.

scanned continuously from 0 to 1 ps, with multiple sweeps for each t_{43} delay. The t_{43} delay was scanned from of 0 to 51 fs in steps of 3 fs. One (T, t_{43}) scan now takes only ~2.3 min compared to 40 min in the 3D scan. The resulting 2D dataset is then Fourier transformed along the t_{43} axis to yield the detection axis (ω_3). The final SRPP spectrum for the rephasing pathways is shown in Fig. 6(a) where a total of 8 T sweeps per t_{43} time point were performed for the reported SNR. Polar solvation dynamics evident from changing 2D line shapes (Fig. 4) is seen as an ultrafast red-shift along the detection axis in Fig. 6(a). Similar to the 3D scan, a three-exponential global fit of the data and the Fourier transform of residuals yield a 2D map (ω_3, ω_T), shown in Fig. 6(c). The corresponding Frobenius map [Fig. 6(b)] calculated over the frequency range within red lines in Fig. 6(a) shows the prominent coherence frequency ω_T = 586 cm^{-1}, consistent with the 2D CMs (Fig. 5). Similar to Fig. 5(b), the Frobenius norm is compared with the noise floor calculated over frequencies marked by gray lines in Fig. 6(a), resulting in SNR comparable to the 2D CMs but with a significantly faster experiment. The corresponding (ω_T, ω_3) map in Fig. 6(c) shows the location of the 586 cm^{-1} mode (vertical dashed line). The location of the main 2D CM peak amplitude [Fig. 5(c)], shown as the dashed horizontal line, is consistent with the corresponding peak location in the SRPP spectrum. Faint amplitudes are seen one vibrational quanta above and below the main peak although with magnitude comparable to the noise floor. The SRPP spectrum demonstrates SNR comparable to 2D CMs but with a significantly improved experimental time. The flexibility of the continuous T scanning approach also allows for more averages, faster scan velocity, the ability to isolate signals based on the T quantum beat phase, and reconstructing the ω_1 axis as well, suggesting that a slower 2D CM experiment may not be that advantageous overall.

D. Compressive sensing enables faster experiment

A comparison between SRPP and 2D experiments for the case of 1 mOD (Fig. 6) suggests that the AOPM approach to fPP for reconstructing ω_1 or ω_3 dimensions separately with significantly faster data collection time may be an effective strategy to improve sensitivity for the lowest ODs. To further pursue this strategy or when 2D CMs are desirable, reduction in the (t_{21}, t_{43}) grid is required even after optimizing T sweep parameters. As an exploratory approach, which rests on the flexibility of continuous T scanning, we extend the idea of biased sampling of uniform signal contours in the (t_{21}, t_{43}) time grid (Sec. II C) to non-uniform sampling. Instead of sampling a uniform grid, we apply a biased exponential sampling (ES) scheme where the separation between the sampled data points increases exponentially with the delay. The ES points are derived using the equation $P_N = \alpha.e^{\beta.N} - c$, where P_N are the sampled points and N is the index number corresponding to each sampled point and constants α = 1.9, β = 0.223, and c = 2 are optimized for the particular system studied here. A schematic of this ES grid is shown in Fig. 7(a). For comparison, a 52 × 52 grid (with 1 fs time steps) is overlaid in the background. Such a grid is only sampled

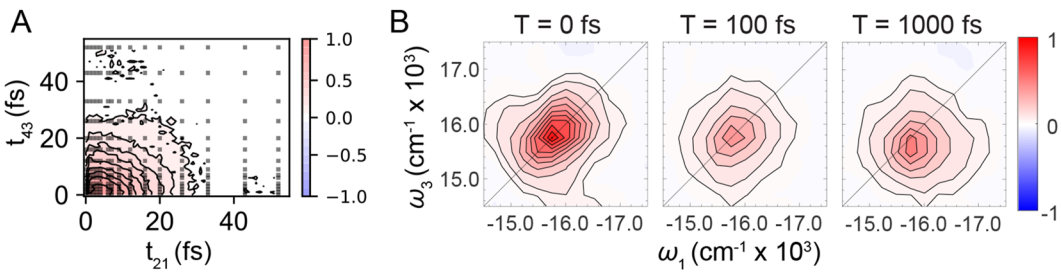

FIG. 7. (a) Exponential sampling (ES) scheme applied on a 52 × 52 dense uniform grid leads to only the 15 × 15 number of points with maximum sampling frequency in the regions where the signal is maximum. The experimentally measured time domain signal for the dense uniform grid is shown as 10% contours in the background. (b) Absorptive 2DES spectra measured at a sample OD of 1.4 mOD reconstructed using a 15 × 15 ES sampled grid at a pump–probe waiting time T of 0 fs, 100 fs, and 1 ps. Contours are drawn at the 5% and 10%–100% in 10% intervals for positive or negative contours.

at the 15 × 15 number of points in the ES scheme, which amounts to a 91% reduction in experimental data collection time.

Reconstruction of a uniform frequency grid starting from non-uniformly sampled time-domain data is, in principle, guaranteed due to the linearity of Fourier transformation. Starting with N ES points, one can write the Fourier transformation from P_N to F_K as $P_N = [iFT]_{N\times K}F_K$, where F_K is defined in the frequency domain and $[iFT]_{N\times K}$ is the inverse Fourier transformation matrix. Such a transformation can be found using compressive sensing (CS) algorithms by minimizing the l_1 norm of F_K. One such method, the spectral projected gradient approach, SPGL1,[66] was employed by Marcus and Aspuru-Guzik *et al.*[23] to reconstruct 2D spectra of rubidium vapor by collecting a dense grid and then non-uniformly sampling the grid to reconstruct the spectrum obtained with the full grid. A similar approach has been demonstrated by Pullerits *et al.*[67]

As a departure from previous approaches, we have used the ES scheme and collected the 15 × 15 grid from an *independent* experiment conducted on a different day such that the uniform and non-uniform data points do not share correlations. In our experience, deriving data points from a denser grid tends to maintain correlations better, leading to a much improved reconstruction. However, such an approach does not translate to an actual reduction in experimental data collection time, which in going from 18 × 18 to 15 × 15 grid is nearly 1/3rd in our approach. The resulting absorptive 2D spectra, with both frequency axes reconstructed using the SPGL1 algorithm applied on the 15 × 15 ES grid, are shown in Fig. 7(b). The sample OD was 1.4 mOD, with equivalent 2D spectra collected from a uniformly sampled 18 × 18 grid shown in Fig. 4 (bottom panel). 2D peak shifts of the order of $\omega_{1,3}$ resolution are evident although features associated with solvation dynamics, such as loss of frequency correlations, and associated changes in 2D line shapes and detection frequency are captured to within the 10%–20% contour level. This is significant in light of the 1/3rd reduction in data collection time for starting sample OD 2–3 orders of magnitude lesser than typical.

A combination of physical undersampling in the AOPM approach and the flexibility of choosing (t_{21}, t_{43}) grid points in the continuous T scanning approach may be promising for spatially resolved fMES measurements. However, further checks such as systematic characterization of the effect of the sampling grid on 2D line shape reconstruction and robustness to noise sources arising from interferometer instabilities, laser drifts, and sample photodamage are required before such applications can be made reliable. Compared to several other implementations[7] of conventional 2DES, fMES is a slow time-domain experiment due to the requirement of sampling all the three time delays. Although CS applications in fMES have been quite sparse,[23,67] our proof-of-concept demonstration suggests that this could be an interesting avenue to explore further, especially for low-photon number light sources, such as entangled photon pairs.[24]

IV. CONCLUSIONS

We have presented a visible WLC-based fMES spectrometer that combines the advantages of physical undersampling and phase-sensitive lock-in detection in the AOPM approach with rapid scanning of the pump–probe delay. Absorptive 2DES spectra and associated polar solvation dynamics features are consistent across a range of ~1–100 mOD, where the lowest sample ODs are ~2–3 orders of magnitude lower than that reported in conventional 2DES approaches. As a measure of sensitivity, suppression of $1/f$ laser noise due to lock-in detection with a fast time-constant and the increased number of T averages enabled by rapid scanning allow us to consistently measure coherent vibrational wavepackets even at the lowest sample ODs. This is especially significant for the measurement of weak signals with dominant probe noise,[19] where ~5% RMS spectral fluctuations across the entire visible WLC bandwidth are typical.[21,22,54] We have also demonstrated a significantly faster 1D experiment with only detection frequency information but with features such as isolation of rephasing and non-rephasing pathways along with quantum beat phase information, not available in conventional pump–probe spectroscopy. A faster experiment with increased T averaging can further improve the SNR at the lowest sample ODs, can provide excitation and detection frequency information separately, and still provide signal pathway isolation similar[68] to that available in a significantly slower 2D CM experiment. Note that a reduction in T scan time is also dependent on the vibrational frequency being sampled, with further room available for a faster T scan velocity.

A continuous pump–probe delay scan per (t_{21}, t_{43}) point offers certain distinct advantages, such as a minimized sample exposure window relevant for spatially resolved measurements on samples susceptible to photo-bleaching; fine T sampling for effective averaging of high-frequency noise, such as sample scatter in the case of conventional 2DES on photosynthetic cells;[5,42] and the ability to choose (t_{21}, t_{43}) time points. The latter feature leverages physical undersampling possible in the AOPM approach and has also allowed us to explore further reductions in experimental time. An exponential sampling scheme biased toward (t_{21}, t_{43}) points where the signal is maximum allows for 1/3rd reduction in data collection time. 2DES spectra reconstructed through compressive sensing show features that are roughly consistent with uniformly sampled spectra, motivating further applications of CS in fMES. Recent demonstration[69] of fMES for the detection of phonon wavepackets in single-layer $MoSe_2$ at room temperature has been quite promising. The advantages of the rapid T scanning approach for high-sensitivity spatially resolved measurements, at lower repetition rates and minimized sample exposure, suggest promising future applications in both action- and coherence-detected microscopies.

SUPPLEMENTARY MATERIAL

See the supplementary material for the details of spot size determination at the sample position, simulation of the two photon autocorrelation signal using an experimental laser spectrum, sample preparation, sample stability over experimental time, pump–probe continuous scan parameters, T zero delay determination, phasing of 2D spectra, field autocorrelation, and fringe modulation depth measurement.

ACKNOWLEDGMENTS

A.S. and S.P. acknowledge the research fellowship from the Indian Institute of Science (IISc). V.N.B. acknowledges the

Inspire fellowship from the Department of Science and Technology. V.T. acknowledges the support from the Infosys Foundation Young Investigator Award. This project was supported, in part, by the Science and Engineering Research Board, India, under Grant Sanction No. CRG/2019/003691, the Department of Atomic Energy, India, under Grant Sanction No. 58/20/31/2019-BRNS, the Department of Biotechnology, India, under Grant Sanction No. BT/PR38464/BRB/10/1893/2020, and the ISRO-STC under Grant Sanction No. ISTC/CSS/VT/468.

AUTHOR DECLARATIONS

Conflict of Interest

The authors have no conflicts to disclose.

Author Contributions

Amitav Sahu: Formal analysis (equal); Methodology (equal); Software (equal); Writing – original draft (equal); Writing – review & editing (equal). **Vivek N. Bhat**: Formal analysis (equal); Methodology (equal). **Sanjoy Patra**: Formal analysis (equal); Methodology (equal); Writing – original draft (equal). **Vivek Tiwari**: Conceptualization (lead); Funding acquisition (lead); Methodology (lead); Software (equal); Supervision (lead); Writing – original draft (equal); Writing – review & editing (equal).

DATA AVAILABILITY

The data that support the findings of this study are available from the corresponding author upon reasonable request

REFERENCES

[1]D. M. Jonas, "Optical analogs of 2D NMR," Science **300**(6 June), 1515–1517 (2003).
[2]W. P. Aue, E. Bartholdi, and R. R. Ernst, "Two-dimensional spectroscopy. Application to nuclear magnetic resonance," J. Chem. Phys. **64**(5), 2229–2246 (1976).
[3]D. Finkelstein-Shapiro, P.-A. Mante, S. Sarisozen, L. Wittenbecher, I. Minda, S. Balci, T. Pullerits, and D. Zigmantas, "Understanding radiative transitions and relaxation pathways in plexcitons," Chem **7**(4), 1092–1107 (2021).
[4]J. Cao, R. J. Cogdell, D. F. Coker, H. G. Duan, J. Hauer, U. Kleinekathöfer, T. L. C. Jansen, T. Mančal, R. J. D. Miller, J. P. Ogilvie, V. I. Prokhorenko, T. Renger, H. S. Tan, R. Tempelaar, M. Thorwart, E. Thyrhaug, S. Westenhoff, and D. Zigmantas, "Quantum biology revisited," Sci. Adv. **6**(14), eaaz4888 (2020).
[5]P. D. Dahlberg, A. F. Fidler, J. R. Caram, P. D. Long, and G. S. Engel, "Energy transfer observed in live cells using two-dimensional electronic spectroscopy," J. Phys. Chem. Lett. **4**(21), 3636–3640 (2013).
[6]J. Dostál, J. Pšenčík, and D. Zigmantas, "In situ mapping of the energy flow through the entire photosynthetic apparatus," Nat. Chem. **8**, 705 (2016).
[7]F. D. Fuller and J. P. Ogilvie, "Experimental implementations of two-dimensional Fourier transform electronic spectroscopy," Annu. Rev. Phys. Chem. **66**(1), 667–690 (2015).
[8]V. Tiwari, "Multidimensional electronic spectroscopy in high-definition - combining spectral, temporal and spatial resolutions," J. Chem. Phys. **154**, 230901 (2021).
[9]S. Roeding and B. Tobias, "Coherent two-dimensional electronic mass spectrometry," Nat. Commun. **9**(1), 2519 (2018).
[10]L. Bruder, U. Bangert, M. Binz, D. Uhl, R. Vexiau, N. Bouloufa-Maafa, O. Dulieu, and F. Stienkemeier, "Coherent multidimensional spectroscopy of dilute gas-phase nanosystems," Nat. Commun. **9**(1), 4823 (2018).
[11]J. A. Cina, "Wave-packet interferometry and molecular state reconstruction: Spectroscopic adventures on the left-hand side of the Schrödinger equation," Annu. Rev. Phys. Chem. **59**(1), 319–342 (2008).
[12]S. Mueller, J. Lüttig, P. Malý, L. Ji, J. Han, M. Moos, T. B. Marder, U. H. F. Bunz, A. Dreuw, C. Lambert, and T. Brixner, "Rapid multiple-quantum three-dimensional fluorescence spectroscopy disentangles quantum pathways," Nat. Commun. **10**(1), 4735 (2019).
[13]P. F. Tekavec, G. A. Lott, and A. H. Marcus, "Fluorescence-detected two-dimensional electronic coherence spectroscopy by acousto-optic phase modulation," J. Chem. Phys. **127**(21), 214307–214327 (2007).
[14]S. Goetz, D. Li, V. Kolb, J. Pflaum, and T. Brixner, "Coherent two-dimensional fluorescence micro-spectroscopy," Opt. Express **26**(4), 3915–3925 (2018).
[15]V. Tiwari, Y. A. Matutes, A. T. Gardiner, T. L. C. Jansen, R. J. Cogdell, and J. P. Ogilvie, "Spatially-resolved fluorescence-detected two-dimensional electronic spectroscopy probes varying excitonic structure in photosynthetic bacteria," Nat. Commun. **9**(1), 4219 (2018).
[16]A. K. De, D. Monahan, J. M. Dawlaty, and G. R. Fleming, "Two-dimensional fluorescence-detected coherent spectroscopy with absolute phasing by confocal imaging of a dynamic grating and 27-step phase-cycling," J. Chem. Phys. **140**(19), 194201 (2014).
[17]J. N. Mastron and A. Tokmakoff, "Fourier transform fluorescence-encoded infrared spectroscopy," J. Phys. Chem. A **122**(2), 554–562 (2018).
[18]D. Agathangelou, A. Javed, F. Sessa, X. Solinas, M. Joffre, and J. P. Ogilvie, "Phase-modulated rapid-scanning fluorescence-detected two-dimensional electronic spectroscopy," J. Chem. Phys. **155**(9), 094201 (2021).
[19]J. A. Moon, "Optimization of signal-to-noise ratios in pump-probe spectroscopy," Rev. Sci. Instrum. **64**(7), 1775–1778 (1993).
[20]G. Auböck, C. Consani, R. Monni, A. Cannizzo, F. van Mourik, and M. Chergui, "Femtosecond pump/supercontinuum-probe setup with 20 kHz repetition rate," Rev. Sci. Instrum. **83**(9), 093105 (2012).
[21]B. Lang, "Photometrics of ultrafast and fast broadband electronic transient absorption spectroscopy: State of the art," Rev. Sci. Instrum. **89**(9), 093112 (2018).
[22]M. Bradler and E. Riedle, "Temporal and spectral correlations in bulk continua and improved use in transient spectroscopy," J. Opt. Soc. Am. B **31**(7), 1465–1475 (2014).
[23]J. N. Sanders, S. K. Saikin, S. Mostame, X. Andrade, J. R. Widom, A. H. Marcus, and A. Aspuru-Guzik, "Compressed sensing for multidimensional spectroscopy experiments," J. Phys. Chem. Lett. **3**(18), 2697–2702 (2012).
[24]J. Lavoie, T. Landes, A. Tamimi, B. J. Smith, A. H. Marcus, and M. G. Raymer, "Phase-modulated interferometry, spectroscopy, and refractometry using entangled photon pairs," Adv. Quantum Technol. **3**(11), 1900114 (2020).
[25]J. Kasprzak, B. Patton, V. Savona, and W. Langbein, "Coherent coupling between distant excitons revealed by two-dimensional nonlinear hyperspectral imaging," Nat. Photonics **5**(1), 57–63 (2011).
[26]T. M. Autry, G. Moody, J. Fraser, C. McDonald, R. P. Mirin, and K. Silverman, "Single-scan acquisition of multiple multidimensional spectra," Optica **6**(6), 735–744 (2019).
[27]E. W. Martin, J. Horng, H. G. Ruth, E. Paik, M.-H. Wentzel, H. Deng, and S. T. Cundiff, "Encapsulation narrows and preserves the excitonic homogeneous linewidth of exfoliated monolayer $MoSe_2$," Phys. Rev. Appl. **14**(2), 21002 (2020).
[28]G. Nardin, T. M. Autry, K. L. Silverman, and S. T. Cundiff, "Multidimensional coherent photocurrent spectroscopy of a semiconductor nanostructure," Opt. Express **21**(23), 28617–28627 (2013).
[29]K. J. Karki, J. R. Widom, J. Seibt, I. Moody, M. C. Lonergan, T. Pullerits, and A. H. Marcus, "Coherent two-dimensional photocurrent spectroscopy in a PbS quantum dot photocell," Nat. Commun. **5**, 5869 (2014).
[30]N. F. Scherer, R. J. Carlson, A. Matro, M. Du, A. J. Ruggiero, V. Romero-Rochin, J. A. Cina, G. R. Fleming, and S. A. Rice, "Fluorescence-detected wave packet interferometry: Time resolved molecular spectroscopy with sequences of femtosecond phase-locked pulses," J. Chem. Phys. **95**(3), 1487–1511 (1991).
[31]D. M. Jonas, "Two-dimensional femtosecond spectroscopy," Annu. Rev. Phys. Chem. **54**, 425–463 (2003).

[32]E. J. Heller, "The semiclassical way to molecular spectroscopy," Acc. Chem. Res. **14**(12), 368–375 (1981).
[33]J. Ryu, S. D. Park, D. Baranov, I. Rreza, J. S. Owen, and D. M. Jonas, "Relations between absorption, emission, and excited state chemical potentials from nanocrystal 2D spectra," Sci. Adv. **7**(22), eabf4741 (2021).
[34]I. Amat-Roldán, I. Cormack, P. Loza-Alvarez, E. Gualda, and D. Artigas, "Ultrashort pulse characterisation with SHG collinear-FROG," Opt. Express **12**(6), 1169–1178 (2004).
[35]G. Stibenz and G. n. Steinmeyer, "Interferometric frequency-resolved optical gating," Opt. Express **13**(7), 2617–2626 (2005).
[36]Y. Coello, V. V. Lozovoy, T. C. Gunaratne, B. Xu, I. Borukhovich, C.-h. Tseng, T. Weinacht, and M. Dantus, "Interference without an interferometer: A different approach to measuring, compressing, and shaping ultrashort laser pulses," J. Opt. Soc. Am. B **25**(6), A140–A150 (2008).
[37]J. K. Ranka, A. L. Gaeta, A. Baltuska, M. S. Pshenichnikov, and D. A. Wiersma, "Autocorrelation measurement of 6-fs pulses based on the two-photon-induced photocurrent in a GaAsP photodiode," Opt. Lett. **22**(17), 1344–1346 (1997).
[38]S. Lochbrunner, P. Huppmann, and E. Riedle, "Crosscorrelation measurements of ultrashort visible pulses: Comparison between nonlinear crystals and SiC photodiodes," Opt. Commun. **184**(1), 321–328 (2000).
[39]E. A. Donley, T. P. Heavner, F. Levi, M. O. Tataw, and S. R. Jefferts, "Double-pass acousto-optic modulator system," Rev. Sci. Instrum. **76**(6), 63112 (2005).
[40]D. Brinks, R. Hildner, F. D. Stefani, and N. F. van Hulst, "Beating spatio-temporal coupling: Implications for pulse shaping and coherent control experiments," Opt. Express **19**(27), 26486–26499 (2011).
[41]S. Pres, L. Kontschak, M. Hensen, and T. Brixner, "Coherent 2D electronic spectroscopy with complete characterization of excitation pulses during all scanning steps," Opt. Express **29**(3), 4191–4209 (2021).
[42]P. D. Dahlberg, P.-C. Ting, S. C. Massey, M. A. Allodi, E. C. Martin, C. N. Hunter, and G. S. Engel, "Mapping the ultrafast flow of harvested solar energy in living photosynthetic cells," Nat. Commun. **8**, 988–994 (2017).
[43]S. Irgen-Gioro, A. P. Spencer, W. O. Hutson, and E. Harel, "Coherences of bacteriochlorophyll a uncovered using 3D-electronic spectroscopy," J. Phys. Chem. Lett. **9**(20), 6077–6081 (2018).
[44]E. Bartholdi and R. R. Ernst, "Fourier spectroscopy and the causality principle," J. Magn. Reson. **11**(1), 9–19 (1973).
[45]D. M. Jonas, "Vibrational and nonadiabatic coherence in 2D electronic spectroscopy, the Jahn–Teller effect, and energy transfer," Annu. Rev. Phys. Chem. **69**(1), 327–352 (2018).
[46]B. Cho, V. Tiwari, R. J. Hill, W. K. Peters, T. L. Courtney, A. P. Spencer, and D. M. Jonas, "Absolute measurement of femtosecond pump–probe signal strength," J. Phys. Chem. A **117**(29), 6332–6345 (2013).
[47]B. Cho, V. Tiwari, and D. M. Jonas, "Simultaneous all-optical determination of molecular concentration and extinction coefficient," Anal. Chem. **85**(11), 5514–5521 (2013).
[48]J. D. Hybl, A. Albrecht Ferro, and D. M. Jonas, "Two-dimensional Fourier transform electronic spectroscopy," J. Chem. Phys. **115**(14), 6606–6622 (2001).
[49]R. J. McIntyre, "Multiplication noise in uniform avalanche diodes," IEEE Trans. Electron Devices **ED-13**(1), 164–168 (1966).
[50]R. Gvishi and R. Reisfeld, "An investigation of the equilibrium between various forms of oxazine-170 by means of absorption and fluorescence spectroscopy," Chem. Phys. Lett. **156**(2), 181–186 (1989).
[51]V. V. Kostjukov, "Photoexcitation of oxazine 170 dye in aqueous solution: TD-DFT study," J. Mol. Model. **27**(11), 311 (2021).
[52]M. Vogel, W. Rettig, U. Fiedeldei, and H. Baumgärtel, "Non-radiative deactivation via biradicaloid charge-transfer states in oxazine and thiazine dyes," Chem. Phys. Lett. **148**(4), 347–352 (1988).
[53]M. S. Zakerhamidi and S. G. Sorkhabi, "Solvent effects on the molecular resonance structures and photo-physical properties of a group of oxazine dyes," J. Lumin. **157**, 220–228 (2015).
[54]A. L. Dobryakov, S. A. Kovalenko, A. Weigel, J. L. Pérez-Lustres, J. Lange, A. Müller, and N. P. Ernsting, "Femtosecond pump/supercontinuum-probe spectroscopy: Optimized setup and signal analysis for single-shot spectral referencing," Rev. Sci. Instrum. **81**(11), 113106 (2010).
[55]D. A. Farrow, E. R. Smith, W. Qian, and D. M. Jonas, "The polarization anisotropy of vibrational quantum beats in resonant pump-probe experiments: Diagrammatic calculations for square symmetric molecules," J. Chem. Phys. **129**(17), 174509 (2008).
[56]V. Butkus, J. Alster, E. Bašinskaitė, R. Augulis, P. Neuhaus, L. Valkunas, H. L. Anderson, D. Abramavicius, and D. Zigmantas, "Discrimination of diverse coherences allows identification of electronic transitions of a molecular nanoring," J. Phys. Chem. Lett. **8**(10), 2344–2349 (2017).
[57]M. Bradler, P. Baum, and E. Riedle, "Femtosecond continuum generation in bulk laser host materials with sub-μJ pump pulses," Appl. Phys. B **97**(3), 561 (2009).
[58]J. Moses, S.-W. Huang, K.-H. Hong, O. D. Mücke, E. L. Falcão-Filho, A. Benedick, F. Ö. Ilday, A. Dergachev, J. A. Bolger, B. J. Eggleton, and F. X. Kärtner, "Highly stable ultrabroadband mid-IR optical parametric chirped-pulse amplifier optimized for superfluorescence suppression," Opt. Lett. **34**(11), 1639–1641 (2009).
[59]W. P. Carbery, B. Pinto-Pacheco, D. Buccella, and D. B. Turner, "Resolving the fluorescence quenching mechanism of an oxazine dye using ultrabroadband two-dimensional electronic spectroscopy," J. Phys. Chem. A **123**(24), 5072–5080 (2019).
[60]R. Zhu, J. Zou, Z. Wang, H. Chen, and Y. Weng, "Electronic state-resolved multimode-coupled vibrational wavepackets in oxazine 720 by two-dimensional electronic spectroscopy," J. Phys. Chem. A **124**(45), 9333–9342 (2020).
[61]J. Brazard, L. A. Bizimana, T. Gellen, W. P. Carbery, and D. B. Turner, "Experimental detection of branching at a conical intersection in a highly fluorescent molecule," J. Phys. Chem. Lett. **7**(1), 14–19 (2016).
[62]M. S. Barclay, J. S. Huff, R. D. Pensack, P. H. Davis, W. B. Knowlton, B. Yurke, J. C. Dean, P. C. Arpin, and D. B. Turner, "Characterizing mode anharmonicity and Huang–Rhys factors using models of femtosecond coherence spectra," J. Phys. Chem. Lett. **13**(24), 5413–5423 (2022).
[63]D. V. Le, J. M. de la Perrelle, T. N. Do, X. Leng, P. C. Tapping, G. D. Scholes, T. W. Kee, and H.-S. Tan, "Characterization of the ultrafast spectral diffusion and vibronic coherence of TIPS-pentacene using 2D electronic spectroscopy," J. Chem. Phys. **155**(1), 014302 (2021).
[64]V. Tiwari, Y. A. Matutes, A. Konar, Z. Yu, M. Ptaszek, D. F. Bocian, D. Holten, C. Kirmaier, and J. P. Ogilvie, "Strongly coupled bacteriochlorin dyad studied using phase-modulated fluorescence-detected two-dimensional electronic spectroscopy," Opt. Express **26**(17), 22327–22341 (2018).
[65]P. Malý and T. Brixner, "Fluorescence-detected pump–probe spectroscopy," Angew. Chem., Int. Ed. **60**(34), 18867–18875 (2021).
[66]E. van den Berg and M. P. Friedlander, "Probing the Pareto Frontier for basis pursuit solutions," SIAM J. Sci. Comput. **31**(2), 890–912 (2009).
[67]Z. Wang, S. Lei, K. J. Karki, A. Jakobsson, and T. Pullerits, "Compressed sensing for reconstructing coherent multidimensional spectra," J. Phys. Chem. A **124**(9), 1861–1866 (2020).
[68]S. S. Senlik, V. R. Policht, and J. P. Ogilvie, "Two-color nonlinear spectroscopy for the rapid acquisition of coherent dynamics," J. Phys. Chem. Lett. **6**(13), 2413–2420 (2015).
[69]D. Li, C. Trovatello, S. Dal Conte, M. Nuß, G. Soavi, G. Wang, A. C. Ferrari, G. Cerullo, and T. Brixner, "Exciton-phonon coupling strength in single-layer $MoSe_2$ at room temperature," Nat. Commun. **12**(1), 954 (2021).